Hydrol. Earth Syst. Sci. Discuss., 11, 8995–9026, 2014
www.hydrol-earth-syst-sci-discuss.net/11/8995/2014/
doi:10.5194/hessd-11-8995-2014

Hydrology and Earth System Sciences
Open Access
Discussions

Multi-scale analysis of bias correction of soil moisture

C.-H. Su and D. Ryu

Department of Infrastructure Engineering, University of Melbourne, Victoria 3010, Australia

Received: 1 July 2014 – Accepted: 16 July 2014 – Published: 29 July 2014

Correspondence to: C.-H. Su (csu@unimelb.edu.au)

Published by Copernicus Publications on behalf of the European Geosciences Union.

Abstract

Remote sensing, in situ networks and models are now providing unprecedented information for environmental monitoring. To conjunctively use multi-source data nominally representing an identical variable, one must resolve biases existing between these disparate sources, and the characteristics of the biases can be non-trivial due to spatiotemporal variability of the target variable, inter-sensor differences with variable measurement supports. One such example is of soil moisture (SM) monitoring. Triple collocation (TC) based bias correction is a powerful statistical method that increasingly being used to address this issue but is only applicable to the linear regime, whereas nonlinear method of statistical moment matching is susceptible to unintended biases originating from measurement error. Since different physical processes that influence SM dynamics may be distinguishable by their characteristic spatiotemporal scales, we propose a multi-time-scale linear bias model in the framework of a wavelet-based multiresolution analysis (MRA). The joint MRA-TC analysis was applied to demonstrate scale-dependent biases between in situ, remotely-sensed and modelled SM, the influence of various prospective bias correction schemes on these biases, and lastly to enable multi-scale bias correction and data adaptive, nonlinear de-noising via wavelet thresholding.

1 Introduction

Global environmental monitoring requires geophysical measurements from a variety of sources and sensors to close the information gap. However, different direct and remote sensing, and model simulation can yield different estimates due to different measurement supports and errors. Soil moisture (SM) is one such variable that has garnered increasing interest due to its influences on atmospheric, hydrologic, geomorphic and ecological processes (Rodriguez-Iturbe, 2000; The GLACE Team et al., 2004;

HESSD
11, 8995–9026, 2014

Legates et al., 2011). It also represents an archetype of the aforementioned problem, where in situ networks, remote sensing and models provide extensive SM information.

In situ networks usually provide point-scale measurements; satellite retrieval of shallow SM at mesoscale footprint of 10–50 km must resort to a homogeneity or dominant-feature assumption; whereas modelled SM depends on the simplified model parameterization, and quality, resolution and availability of forcing data. Subsequently, the spatial (lateral and vertical) variability of SM can lead to systematically different measurements regarded as *biases*. Descriptive or predictive spatial SM statistics can be used to relate point-scale to mesoscale estimates (Western et al., 2002), but in situ data is often limited to describe spatial heterogeneity of SM. Yet, without bias correction, it is not possible to conduct meaningful comparisons between in situ, satellite-retrieved and modelled SM for validation (Reichle et al., 2004) and optimal data assimilation (Yilmaz and Crow, 2013). Standard bias correction methods have now increasingly being applied to SM assimilation in land (Reichle et al., 2007; Kumar et al., 2012; Draper et al., 2012), numerical weather prediction (Drusch et al., 2005; Scipal et al., 2008a) and hydrologic models (Brocca et al., 2012). Reichle and Koster (2004) proposed to match statistical moments of the data while linear methods based on simple regression and matching dynamic ranges have also been considered (e.g., Su et al., 2013). But these methods can induce artificial biases as the error statistics were ignored; this also suggests a connection that the issue of bias correction is inseparable from that of error characterisation (Su et al., 2014).

Triple collocation (TC) (Stoffelen, 1998), which is a form of instrument-variable regression (Wright, 1928; Su et al., 2014), is increasingly being used to address these issues in oceanography (Caires and Sterl, 2003; Janssen et al., 2007) and hydrometeorology (Scipal et al., 2008b; Roebeling et al., 2013). In particular, it was used to estimate spatial point-to-footprint sampling errors (Miralles et al., 2011; Gruber et al., 2013), and correct biases in SM (Yilmaz and Crow, 2013). Based on an affine signal model and additive orthogonal error model, it assumes that representativity differences are manifested as additive and multiplicative biases. But these assumptions may

HESSD
11, 8995–9026, 2014

have limited validity, as the temporal behaviour of SM may vary across different spatial scales, driven by a continuum of localised and mesoscale influences (e.g., Entin et al., 2000; Mittelbach and Seneviratne, 2012). Specifically, the coupling of SM with precipitation and evaporative losses (controlled by temperature, humidity, wind speed) varies across spatial scales. This can be more pronounced at places where surface hydrological features (e.g., topography, infiltration rate and storage capacity) are highly heterogeneous. Thus, the biases are likely to be non-systematic across short and long time scales at different spatial scales and errors are non-white, undermining the utility of the affine model. One possible remedy is to apply bias correction, either TC or statistical-moment matching, only to anomaly timeseries (Miralles et al., 2011; Liu et al., 2012; Su et al., 2014), but it remains unclear how these methods affect the signal and noise components in the corrected data.

Given the possible (time) scale dependency in biases and errors, we propose an extension to TC analyses to include wavelet-based multi-resolution analysis (MRA) (Mallat, 1989) as a framework to (1) provide a fuller description of the temporal scale-by-scale relationships between coincident data sets; (2) study the influence of various prospective bias correction schemes; and (3) achieve multi-scale bias correction. To avoid excessive changes in the noise characteristics upon correction, TC can be further combined with the wavelet thresholding to (4) achieve nonlinear, data adaptive de-noising (Donoho and Johnstone, 1994). The techniques were applied to SM data from in situ probe, satellite radiometry and land-surface model, but the proposed methods are general enough to be applied to other geophysical variables.

The paper is organised as follows. Section 2 presents the study area over Australia and the SM data sets used in our pilot studies. Section 3 explains the theoretics behind MRA and applies it to SM, following by examination of scale-by-scale statistics in Sect. 4. Section 5 presents a new joint MRA-TC analysis framework, which is then applied to examine the influence of different bias correction schemes in Sect. 6. Importantly, both Sects. 4 and 6, using wavelet correlation, wavelet variance and scale-level TC analyses, provide evidence to support the need to extend traditional bulk and

HESSD
11, 8995–9026, 2014

anomaly-based analyses. Section 7 demonstrates the use of wavelet thresholding to de-noise satellite SM. Section 8 offers our concluding remarks.

2 Study areas and data sets

We consider in situ, satellite-retrieved and modelled SM over Australia. For an in-depth study, we consider point-scale and pixel-scale SM estimates at *K1* monitoring site (147.56° longitude, −35.49° latitude) situated at Kyeamba Creek catchment, southeast Australia (Smith et al., 2012; Su et al., 2013). The in situ SM (*INS* as shorthand) was sampled at 30 min intervals, 0–8 cm depth using a time-domain interferometer-based Campbell Scientific 615 probe during November 2001–April 2011. The region experiences a temperate (Cfb) climate characterised by seasonally uniform rainfall but variable evapotranspiration forcing, so that SM varies between dry in summer (December–February) to wet in winter (June–August). The Creek is located on gentle slopes with rainfed cropping and pasture, and the soil varies from sandy to loam. Figure 1 illustrates the land cover, elevation, monthly rainfall accumulation (from 2002–2011), and clay content over the region.

The satellite SM was retrieved by AMSR-E (Advanced Microwave Scanning Radiometer for Earth Observing System; *AMS*) of the AQUA satellite. The retrieval is based on an inversion of the forward radiative transfer model of a vegetation-masked soil surface, relating observed brightness temperature to soil dielectric constant estimates. A dielectric mixing model is then used to related the dielectric constant to volumetric SM. The version 5 combined C/X-band $1/4^\circ \times 1/4^\circ$ resolution, half-daily ($\sim$1.30 a.m./p.m. local time) product (July 2002–October 2011) is based on Land Parameter Retrieval Model (Owe et al., 2008). C-band (X-band) has a shallow sampling depth of $\sim$1–2 cm ($\sim$5 mm). Given the 1–2 day revisit times of the satellite, there is significant number of missing values in AMS data. However, we found that (not shown) over 99 % of the gaps over Australia are $\leq$ 1.5 day long. For use in wavelet analysis (Sect. 4), a one-dimensional (1-D in time) interpolation algorithm based on discrete

HESSD
11, 8995–9026, 2014

cosine transform (Wang et al., 2012) was applied to infill gaps of lengths ≤ 5 days in AMSR-E.

The modelled SM is taken from MERRA (Modern Era Retrospective-analysis for Research and Applications) – Land produced by Catchment land surface model GEOS version 5.7.2. The MERRA atmospheric re-analysis is driven by a vast collection of in situ observations of atmospheric and surface winds, temperature, and humidity, and remote sensing of precipitation and radiation (Rienecker et al., 2011). The MERRA land-only fields were post-processed by reintegrating a revised Catchment model with more realistic precipitation forcing to produce the MERRA-Land (*MER* as shorthand) data set (Reichle et al., 2011). The resultant SM field corresponds to the hourly averages of the uppermost layer (0–2 cm) and is gridded on a $2/3^{\circ} \times 1/2^{\circ}$ grid.

The three data are co-located spatially via nearest neighbour and temporally at around the satellite overpass times of 1.30 a.m./p.m. Their timeseries are plotted in blue in the first panels of Fig. 2. While co-located, the three methods observed SM dynamics over different locations and areas of the catchment (Fig. 1), due to differences in their pixel resolutions and alignments.

Continental-scale AMS and MER data over Australia are also considered. The continent has great variability in climatic and land surface characteristics. The most of the northern regions experience a Tropical Savannah (Aw) Köppen-Geiger climate as classified by Peel et al. (2007), the central Australia is largely arid desert (BWh), and eastern mountainous areas has a Temperate climate with no dry seasons (Cf). The south-western regions similarly have a Temperate climate, but with dry summer (Cs). These temperate regions have higher vegetation, compared to the tropical north with moderate vegetation cover.

3 Multi-scale decomposition of soil moisture

The observed SM in Fig. 2 exhibit long-term cycle of wet and dry years due to El-Niño Southern Oscillation, seasonal and diurnal cycles originating from the fluctuations

HESSD
11, 8995–9026, 2014

in vegetation and solar radiation, and experiences transient decay from various loss mechanisms, and abrupt increase from individual rainfall events. Their influences on observed SM can vary with the measurement methods. To unravel these differences, we turn to wavelets as the analysing kernels to study variability at individual broad-to-fine time scales. The *scale* under investigation is *temporal* for the rest of the paper, unless stated otherwise.

The 1-D orthogonal discrete wavelet transform (DWT) enables MRA of a timeseries $p(t)$ of dyadic length $N = 2^J$ by providing the mechanism to go from one resolution to another via a recursive function

$$p_{j-1}^{(a)}(t) = p_j^{(a)}(t) + p_j(t), \tag{1}$$

with expectation values $E(p_j^{(a)}) = E(p) = \mu_p$ and $E(p_j) = 0$. The integer $j \in [1, J]$ labels the scale of analysis with $j = 1$ (J) denoting the finest (coarsest) scale, and serves to define a spectral range in a spectral analysis. The recursion therefore relates an approximation or coarse representation $p_j^{(a)}$ of the signal at one resolution to that at a higher resolution $p_{j-1}^{(a)}$ by adding some fine-scale detail denoted by p_j. This leads to a multi-resolution decomposition of p as,

$$p(t) = p_{j_0}^{(a)}(t) + \sum_{j=1}^{j_0} p_j(t) \tag{2}$$

$$= \sum_{k=1}^{n_{j_0}} p_{j_0 k}^{(a)} \phi_{jk}(t) + \sum_{j=1}^{j_0} \sum_{k=1}^{n_j} p_{jk} \psi_{jk}(t) \tag{3}$$

under j_0 levels of decomposition. Loosely speaking, for a half-daily timeseries, the *detail timeseries* p_j for $j = 1, 2, 3, \ldots$ corresponds to (fine-scale) dynamics observed at 1 day (1d), 2d, 4d, etc, time scale, while the *approximation timeseries* $p_j^{(a)}$ at

HESSD
11, 8995–9026, 2014

$j = 1,2,3,\ldots$ contains (broad-scale) dynamics at scales longer than 1d, 2d, 4d, etc. In Eq. (3), each of these components is further decomposed into a linear summation of $n_j = N/2^j$ number of basis functions ϕ_{jk} and ψ_{jk} with scale of variability 2^j and temporal location $k2^j$. The weighting or wavelet coefficients, determined via DWT of p, measure the similarity between p and the bases via the inner products $p_{jk}^{(a)} \equiv \langle p, \phi_{jk} \rangle$ and $p_{jk} \equiv \langle p, \psi_{jk} \rangle$. Hence the coefficients indicate changes on a particular scale and location and enable the above scale-by-scale decomposition. Note that the bases as defined in $L^2(R)$ space and satisfy orthonormality conditions prescribed by $\langle \phi_{jk}, \phi_{j'k'} \rangle = \delta_{jj'}\delta_{kk'}$, $\langle \psi_{jk}, \psi_{j'k'} \rangle = \delta_{jj'}\delta_{kk'}$, $\langle \phi_{jk}, \psi_{j'k'} \rangle = 0$, where δ is Kronecker delta function. For detailed expositions of the mathematical theory of wavelets and MRA, consult Daubechies (1992) and Mallat (1989).

The detail and approximated timeseries of Kyeamba's SM are illustrated in subsequent panels of Fig. 2, analysed using the Daubechies $D(4)$ wavelet for $j_0 = 8$. At finest scales $j = 1$–2 (1–2d), the details show variability due to rainfall wetting, and over the next set of scales $j = 2$–6 (2–32d) they describe transient moisture loss. The $p_8^{(a)}$ ($\geq$ 64d) component accounts for several scales of fluctuations over seasonal, interannual, and long-term time scales. The differences between the details of the three SM are apparent at finest scales, with AMS and MER showing greater variability and amplitude compared to INS. However the similarity of their temporal patterns, in both details and approximations, grows with increasing scales $j > 3$ (see also Fig. 3). Fitting a trend line to their coarsest scale approximation series reveals that the AMS observes an increase of SM of $0.16\,m^3\,m^{-3}$ over a 10 year period, MER observes a modest $0.08\,m^3\,m^{-3}$ increase, while INS shows insignificant change ($-0.001\,m^3\,m^{-3}$). The differences in dynamic ranges of their detail and approximation timeseries, together with their mismatch in shape and trend, are indicative of multiplicative biases and noise.

HESSD
11, 8995–9026, 2014

4 Multi-scale statistics

MRA enables direct comparisons between any two representations $p = \{X, Y\}$ of a given variable f (such as SM) at various temporal scales independently, owing to the orthonormal properties of wavelet bases. It also offers an additional degree of freedom in temporal positions (using the index k) to allow better representation of local variability. By subsetting the wavelet coefficients over certain range of k values, non-stationary statistics can also be examined. However in this work, we consider only variability across j and assume stationarity at each scale and performed Pearson linear correlation R and variance analyses (see Appendix A) of the Kyeamba's INS, AMS and MER SM (as p in Eq. 2) detail and approximation timeseries in Fig. 3.

For the detail timeseries (Fig. 3a), the correlations between the three data are low at finest scales ($R < 0.2$) but generally improves with scale ($R > 0.5$), as noted previously. There is however no data-pair that shows consistently higher R than other pairs: $R(\mathrm{INS}_j, \mathrm{AMS}_j) > R(\mathrm{INS}_j, \mathrm{MER}_j)$ at coarser scales j = 4–6,8 whereas $R(\mathrm{INS}_j, \mathrm{MER}_j)$ is highest at other scales.

Comparing their approximation timeseries (Fig. 3b), R between AMS and MER are higher than the other two pairs, ranging from ($j = 2$) 0.8 to 0.92 ($j = 8$), largely due to the strong correlation between their respective p_8 and $p_8^{(a)}$. But the bulk correlation R(INS,AMS) is lower than INS-MER pair due to the contribution of noisy AMS_1 to the makeup of AMS. In other words: on one hand, AMS and MER both show skill in representing some aspects of the in situ SM temporal variability; on the other hand, stronger AMS-MER correlations at coarsest (temporal) scales and their mesoscale spatial resolutions would indicate lesser representativeness of in situ measurement at these spatio-temporal scales.

Next, Fig. 3c plots their wavelet spectra that decompose total variance var(p) into individual scales. The standard deviation (std) statistics are presented. The three data show clear differences in their std profile, both in the fine and coarse scales. Both noise and/or multiplicative biases are possible contributing factors such that noise can

HESSD
11, 8995–9026, 2014

inflate the variance while biases can cause suppression or inflation. Following the visual inspection of Fig. 2 and the noted weak correlations $R(\mathrm{INS}_j, \mathrm{AMS}_j)$ and $R(\mathrm{INS}_j, \mathrm{MER}_j)$ at small j, it can be argued that there is significant noise in AMS (for j = 1–3) and MER (j = 1). This in turn leads to their larger std c.f. INS. At coarser scales where R values are significantly higher, the differences in std may be attributed to multiplicative biases. For instance for their p_8 and $p_8^{(a)}$ components, AMS and MER shows larger std and thus positively biased relative to INS.

Figure 4 extends the variance and correlation analyses between AMS and MER to the Australian continent using their coincident data from the period July 2002–October 2011. The spatial maps of std differences (Δstd) and correlations show significant variability in the statistics with time scales and spatial locations. At the finest scale j = 1, the similarity between the difference map (Fig. 4a) and TC-derived error map of AMSR-E (see Fig. 6a in Su et al., 2014) in terms of spatial variability and the low AMS-MER correlations (Fig. 4f) support our observation that the detail timeseries AMS_1 is noise-dominated. By contrast, owing to strong correlation $R \sim 0.6$–0.9 (Fig. 4g and h) at the coarse scales, the causes for Δstd (Fig. 4c and d) are related to biases. In particular at $j > 8$, Δstd map in Fig. 4d also suggests possible association between biases and climatology or land cover characteristics, with negative biases dominating northern tropical (Aw) and semi-arid (BS) regions, and positive biases in temperate, vegetated regions (Cs and Cf) over southeastern and southwestern Australia. The visual comparisons between scale-level Δstd with bulk Δstd enable stratification of the continent to central arid regions of higher noise identified in j = 1 and 2 and temperate (tropical) regions with positive (negative) bias seen at coarser scales.

5 Joint MRA-TC analysis

In order to quantify observed differences between the data, we propose a *scale-dependent* linear model: a multi-scale (MS) model that distinguishes the signal components of the two data X and Y via a set of positive scaling coefficients $\alpha_{p,j}$, α'_p and

HESSD
11, 8995–9026, 2014

assumes an additive and zero-mean independent but non-white noise model $\epsilon(t)$,

$$p'(t) = \alpha'_p f'(t) + \epsilon'(t), \tag{4}$$

$$p_j(t) = \alpha_{p,j} f_j(t) + \epsilon_{p,j}(t), \tag{5}$$

for $p' = p^{(a)}_{j_0} - E(p)$ and $f = f' - E(f)$. The signal and noise components have also been decomposed into their multi-resolution forms. The differences in the values of the scaling coefficients between data, i.e. $\alpha_{X,j} \neq \alpha_{Y,j}$, signify multiplicative biases at individual scales. To see this, we express their mean-squared deviation $\mathrm{MSD} \equiv E[(Y - X)^2]$ in terms of variables in Eqs. (4) and (5) to arrive at,

$$\mathrm{MSD} = (\mu_X - \mu_Y)^2 + \sum_j^J \left[(\alpha_{Y,j} - \alpha_{X,j})^2 \mathrm{var}(f_j) + \mathrm{var}(\epsilon_{X,j}) + \mathrm{var}(\epsilon_{Y,j})\right]. \tag{6}$$

The first term is the additive bias, and the summation consists of scale-specific multiplicative biases proportional to $(\alpha_{X,j} - \alpha_{Y,j})^2$ and noise contributions from each data.

Importantly the model allows for different scaling coefficients between scales, i.e. $\alpha_{p,j} \neq \alpha'_{p,j}$ for $j \neq j'$, as a form of non-linearity with f. The equality $\alpha_{p,j} = \alpha'_p = \alpha_p$ is therefore a special case of (bulk) linearity. As our focus of the above model is the multiplicative biases and noise, for convenience of notations, we remove the mean of the X and Y prior to MRA and bias correction. Furthermore, without the loss of generality, we choose X as the reference henceforth and let $\alpha_{X,j}, \alpha'_X = 1$.

By using a third independently-derived representation (Z) of f, TC enables estimation of the required scaling coefficients and noise std($\epsilon_{p,j}$) (Appendix B). As we will see later, these estimates are needed for bias correction and de-noising. Within the operating assumptions of TC, TC estimates are unbiased; that is, the estimated $\hat{\alpha}_{Y,j} = \alpha_{Y,j}$ in probability. However TC's superiority is dependent on the availability of a strong instrument and large sample for statistical analyses (Zwieback et al., 2012; Su et al., 2014). Standard linear estimators, namely ordinary least-square (OLS) regression and

HESSD
11, 8995–9026, 2014

variance-matching (VAR), can be considered as substitutes, although they are biased estimators when X and Y are both noisy (Yilmaz and Crow, 2013; Su et al., 2014), e.g., OLS yields $\hat{\alpha}_{Y,j} < \alpha_{Y,j}$. In summary, we propose that combining these estimators with MRA via the MS model enables investigation into the distribution of the biases and noise over j, and their response to various bias correction schemes.

6 Multi-scale analysis of bias correction

Consider now the bias correction of Y to "match" X. Different interpretations of a "match" and assumptions about signal and noise statistics lead to different bias correction schemes:

– *Bulk linear rescaling* assumes bulk linearity between X and Y so that the correction equation is

$$Y^* = \frac{Y}{\hat{\alpha}_Y}, \tag{7}$$

where $\hat{\alpha}_Y$ is ideally given by TC. When the bulk linearity is satisfied, this approach ensures that the statistical properties (std and higher moments) of the signal components in X and Y^* are identical. Linear rescaling using $\hat{\alpha}_Y$ values estimated by OLS and VAR matching have previously been considered by e.g., Su et al. (2013); but due to error-in-variable biases, they can induce artificial case even if the bulk linearity condition is valid.

– *Bulk cumulative distribution function (CDF) matching* assumes nonlinearity between X and Y and transforms Y^* so that (Reichle and Koster, 2004),

$$\mathrm{cdf}(Y^*) = \mathrm{cdf}(X), \tag{8}$$

where cdf(∘) computes the CDF. This ensures that the mean, std, and higher statistical moments of X and Y^* are identical, but the statistical properties of their

HESSD
11, 8995–9026, 2014

signal and noise components that make up X and Y^* are not necessarily identical. In particular, when the relative signal and noise statistics in the two data are different, CDF matching leads to artificial biases between the signal components in X and Y^*. As with VAR matching of first two moments, the CDF counterpart is expected to contain extraneous contribution of the error variances in the mapping of the second moment, as well as at higher moments (Su et al., 2014). The issue can be exacerbated by variable signal and error statistics at different scales.

– *Anomaly/seasonal (A/S) linear rescaling* allows biases between X and Y to be different at two scales of variation. In practice, the useful information content in observations is primarily based on their representation of anomalies, where observations are assumed into a particular land surface model's unique climatology (Koster et al., 2009). The correction is therefore limited to the anomalies, although other components (e.g., seasonal fluctuation and long-term trend) may be preserved to validate model prediction. Here the linear correction using TC estimator is applied to match the characteristics of each component – anomaly (i = A) and seasonal (S) – separately, so that the corrected Y has the form,

$$Y^* = Y^*_{\mathrm{S}} + Y^*_{\mathrm{A}}, \tag{9}$$

with $Y^*_i = Y_i/\hat{\alpha}_{Y_i}$ for $i \in \{\mathrm{S},\mathrm{A}\}$. In one approach, p_{S} is computed using moving window averaging of multiyear data within window size of 31 days centered on a given day of year (Miralles et al., 2011), so that inter-annual cycles and long-term trends are retained in p_{A}. In an alternative approach (Albergel et al., 2012), a sliding 31 day window is used such that $p_{\mathrm{A}} \approx \sum_{j=1}^{6} p_j$ for half-daily timeseries. In this work, the former, more conventional approach was taken.

– *A/S CDF matching* applies CDF matching to anomaly and seasonal components separately as per Eq. (9) but with $\mathrm{cdf}(Y^*_i) = \mathrm{cdf}(X_i)$. The application of CDF matching to the anomaly component of soil moisture data was considered by Liu et al. (2012).

HESSD
11, 8995–9026, 2014

– *Multi-scale (MS) rescaling* is the direct consequence of the MS model where information in Y is rescaled at individual scales,

$$Y^* = \frac{Y'}{\hat{\alpha}'_Y} + \sum_{j=1}^{j_0} \frac{Y_j}{\hat{\alpha}_{Y,j}}. \quad (10)$$

In relation to Eq. (6), this approach eliminates that the multiplicative terms in the summation. It is obvious that bulk and A/S linear correction schemes are special cases of MS rescaling where information from multiple scales are aggregated and corrected jointly. Other aggregations of the information from different subsets of scales are also possible, but they will similarly be conceived based on one's understanding or assumptions of the underlying specific processes driving SM dynamics. Investigations into suitable aggregations are beyond the scope of this work, hence we implemented the most elaborate decomposition. If joint linearity exists between two or more scales, their $\alpha_{Y,j}$ values will be similarly-valued for use in Eq. (10).

For illustrations, we correct the biases in AMS and MER SM with respect to INS SM at Kyeamba using the above schemes. Using the above notations, AMS and MER are treated as Y and INS as X. MRA-TC was applied to observe their consequences. The "true" values of the scaling coefficients $\alpha_{Y,j}$ (before correction) and $\alpha_{Y^*,j}$ (after) were estimated using TC. But where TC estimates could not be retrieved (j = 1–2) due to negative correlation amongst the data triplet (e.g., resulting from significant noise and weak instrument), OLS-derived (under) estimates serve as a guide. Similarly the total std is a guide for error std in these cases.

Figure 5a shows the MRA of the biases and noise in the pre-corrected data. The upper panel illustrates considerable variability in $\hat{\alpha}_{Y,j}$ across the scales, ranging from 0.5–1.8 for AMS, and 0.5–1.4 for MER. In particular their $\hat{\alpha}'_Y$ and $\hat{\alpha}_{Y,8}$ are significantly deviated from 1 and are responsible for the larger std (c.f. INS) observed in Fig. 3c. Biases also exist at almost all other scales of AMS and MER. In the lower panel, the

HESSD
11, 8995–9026, 2014

values std($\varepsilon_{Y,j}$) relative to std(Y_j) indicate the dominance of noise in the small scales j = 1–3. This explains the low R values between AMS (and MER) and INS in Fig. 3a. Furthermore, the signal-to-noise ratios are variable with scales and data sets, highlighting the importance of using a correction scheme that takes the signal-vs.-noise statistics into considerations. TC-based scheme is limited to the linear case and CDF scheme ignores such a variability.

Within the paradigm of the MS model and Eq. (6), the goal of bias correction is to minimize the difference $|\alpha_{Y,j} - 1|$. The MRA of the corrected AMS and MER (as Y^*) are shown in Fig. 5b–f. In addition we assess the level of agreement between corrected AMS and INS timeseries in Table 1 using their root-mean-squared deviation (RMSD) and correlation R. The timeseries plots are shown in Fig. 6 to support interpretations. These additional results focus on the AMS-INS pair that best illustrates the influence of noise. It is of note that for the MS scheme where the scaling coefficients cannot be estimated for j = 1–2 by TC, CDF matching is applied to these scales.

The results of bulk, A/S and MS linear rescaling can be readily interpreted. In particular, for bulk (Fig. 5b) and A/S linear (Fig. 5d) rescaling, the estimated scaling coefficients, namely $\hat{\alpha}_Y$ and $\hat{\alpha}_{Y_j}$, used in their implementations are greater than unity for both AMS and MER. This leads to the suppression of the associated signal, as well as noise, components. For AMS, the bulk linear scheme corrects the coarse-scale bias in $Y_8^{(a)}$ component and rescales the noise variance, reducing RMSD from 0.09 $m^3\,m^{-3}$ to 0.06 $m^3\,m^{-3}$. However the fine-scale biases in Y_j are still present, and increased at some scales, e.g. at j = 4, 7 for AMS. Additionally for A/S linear rescaling, R(AMS,INS) value does not change significantly and the noise are still clearly visible in Fig. 6b and d.

By construction, MS rescaling enables bias correction at all scales, as demonstrated in Fig. 5f. The use of $\hat{\alpha}_{Y,j}$ ($j \geq 3$) values from Fig. 5a in its implementation eliminates biases at respective scales, but we also observed noise amplification in AMS at j = 3, 7 and in MER at j = 3–6 because $\hat{\alpha}_{Y,j} < 1$. Indeed it is evident from Eq. (6) that it is possible to increase the noise variance and MSE when reducing the bias component

HESSD
11, 8995–9026, 2014

of the MSE. This in turn leads to larger disagreement between INS and AMS in terms of RMSD and R, and the increased amplitudes of the noise in AMS in Fig. 6f.

The bulk and A/S CDF methods produced very similar results with each other, and also with their linear counterparts. There are signal and noise suppression but retain the scale-level biases. The signal components of Y^* are negatively biased at $j = 3$–7 and positively biased at $j = 8$. The CDF-corrected AMS shows slightly better RMSD and R with INS, owing to the reduced noise variance and a reduced bias at $Y_8^{(a)}$.

In summary, the MRA of the bulk and A/S schemes highlights the deficiency of using a correction scheme that does not take into account the scale variability of bias and the differences in error statistics between the two data. The improvements in RMSD and correlation between the corrected Y^* and the reference X are somewhat superficial, masking the fact that the bias correction is limited to the coarsest scales. On the other hand, the A/S-based and MS methods can modify the original error profiles in the data across the scales, by amplifying (or suppressing) errors in individual components (either Y_j, Y_S, or Y_A) with less-than (greater-than) unity pre-correction α's. Therefore arguably, none of these methods is entirely satisfactory, in manners of not removing the multiplicative biases completely and/or changing error characteristics. The task of bias correction may therefore be seen as inseparable from that of noise reduction when considering MS (or A/S) bias correction, unless certain components in MRA were explicitly ignored.

7 Combining bias correction with wavelet de-noising

The last example presents an impetus to consider noise removal prior to bias correction. Critically, TC provides noise and signal estimates that can be used for de-noising through thresholding of wavelet coefficients p_{jk}. The basic rationale for wavelet thresholding (WT) is that insignificant detail coefficients are likely due to noise while significant ones are related to the signal component. Thus a coefficient is eliminated if its magnitude is less than a given threshold λ_p; otherwise it is modified according

HESSD
11, 8995–9026, 2014

to a transformation function $\Gamma(p_{jk})$ to remove the influence of the noise (Donoho and Johnstone, 1994).

One commonly-used transformation is soft thresholding (Donoho, 1995), where the coefficients are modified according to,

$$\Gamma_{\lambda_p}(p_{jk}) = \text{sign}(p_{jk})\max(|p_{jk} - \lambda_p|, 0). \quad (11)$$

Such de-noising filters have near-optimal properties in the minmax sense. We follow *BayesShrink* rule of Chang et al. (2000) to define a set of scale-dependent threshold values using

$$\lambda_{p,j} = \frac{\text{var}(\epsilon_{p,j})}{\alpha_{p,j}\text{std}(f_j)} \quad (12)$$

where the variances are provided by TC (Appendix B). This choice of threshold is near-optimal under the assumption that the signal is generalised Gaussian distributed and the noise is Gaussian. When the threshold value for $j = 1$–2 could not be estimated using TC, CDF matching was applied. While TC is an ideal error estimator, alternative estimators for the threshold values are also available to make the de-noising a stand-alone process (Donoho and Johnstone, 1994; Donoho, 1995). The de-noised time-series is therefore constructed via inverse DWT of the modified coefficients, and can be subsequently corrected for biases. Combining with the MS bias correction scheme, a biased-corrected, de-noised data is generated via,

$$Y^* = \frac{Y'}{\hat{\alpha}'_Y} + \sum_{j=1}^{j_0}\sum_{k=1}^{n_j} \frac{\Gamma_{\lambda_{p,j}}(Y_{jk})}{\hat{\alpha}_{Y,j}}\psi_{jk}. \quad (13)$$

The prescription, which is essentially a two-stage operation, was applied to AMS for comparisons with the previous results. The first stage of de-noising leads to smoothing of the timeseries and improved R with INS by 0.05. The actual SM variability has

HESSD
11, 8995–9026, 2014

become more apparent in Fig. 6g. Over-smoothing can occur due to our inability to properly distinguish signal from noise in AMS_1 and AMS_2 where the signal-to-noise ratio is very low. However without the second stage of bias correction, the dynamic ranges of de-noised AMS and INS are visibly different, such that the improvement in RMSD with INS is limited. Combining WT and MS leads to improvement in both metrics of RMSD = 0.048 $m^3 m^{-3}$ and R = 0.711, with Fig. 6h confirming that the reduced noise was not amplified by the MS rescaling.

8 Conclusions

This work combines MRA and TC in a new analysis framework with increased capacity to provide a more comprehensive view of the inter-data relations at short and long time scales. TC (or CDF) rescaling can be exploited at individual scales to reduce scale-specific multiplicative biases, and provide "prior" knowledge of noise for calibrating a WT filter. As a demonstration-of-principle, these methods are applied to SM data from in situ and satellite sensors and a land surface model. Using MRA, we found that the three data exhibit significantly different wavelet spectra. At fine scales, the contribution of noise is most prominent, undermining the correlation between the data sets. By contrast, the biases are most apparent at coarse scales. Further, these biases are non-systematic across time scales at the study region and across spatial locations over Australia. And, the signal-to-noise ratios vary with scales and between the various data, pointing to the need to use correction schemes that are capable of handling such complexities.

These observations raised concerns about the possible inadequate treatment of SM data in the linear regime, even with anomaly/seasonal decomposition. Scale-by-scale linear rescaling based on a MRA-TC analysis framework offers a more comprehensive treatment of different biases at different scales, but error characteristics are found to be modified by variable rescaling and can lead to undesirable noise amplification. The method of removing biases and noise at individual scales offers a remedy, although

HESSD
11, 8995–9026, 2014

few caveats should be noted. First, TC analysis requires a strong instrument and large sample, and in cases where these prerequisites are not met, we resort to sub-optimal estimation and rescaling methods. Second, the issue of non-stationarity in errors and scaling has not been addressed so far, and this can lead to biased estimates of the correction parameters for rescaling and de-noising. Despite this, DWT offers additional degree of freedom in translation parameter k to accommodate non-stationarity. Third, given the theoretic viewpoint presented in this work, further evaluations based on assimilation of data treated by different schemes are still warranted to assess their practical impacts. Notwithstanding these factors, MRA-TC analysis can be an important tool to allow better characterisation of the inter-sensor differences and to develop more effective strategies in harmonising a broad range of observational data records in oceanography and hydrometeorology.

Appendix A: Wavelet statistical analysis

MRA enables the (bulk) variance var(p) of a timeseries p to be decomposed into wavelet variances var(p_j) at different scales j. Analogous to a Fourier spectrum, the expansion of var(p) yields a wavelet spectrum and is given by,

$$\mathrm{var}(p) = \sum_{j=1}^{J} \mathrm{var}(p_j) \tag{A1}$$

$$= \mathrm{var}(p_{j_0}^{(a)}) + \sum_{j=1}^{j_0} \mathrm{var}(p_j) \tag{A2}$$

where the variance of the approximation timeseries $p_{j_0}^{(a)}$ can be expressed in terms of that of the detail timeseries p_j.

Similarly, wavelet covariance cov(X_j, Y_j) at a given j indicates the contribution of covariance between two timeseries (X, Y) at that scale. Specifically, the wavelet

HESSD
11, 8995–9026, 2014

covariance at scale j can be expressed as,

$$\mathrm{cov}(X_j, Y_j) = \frac{1}{n_j} \sum_{k=1}^{n_j} X_{jk} Y_{jk}, \tag{A3}$$

noting that there is an equivalence of computing (co)variance in the wavelet and time domains. To exclude the boundary influence of a finite-length timeseries and missing values in the timeseries, an estimator of the wavelet covariance can be constructed by excluding the coefficients affected by the boundaries and gaps, followed by renormalisation. In the paper, we find it more intuitive to report the wavelet correlation, namely,

$$R(X_j, Y_j) = \frac{\mathrm{cov}(X_j, Y_j)}{\sqrt{\mathrm{var}(X_j)\mathrm{var}(Y_j)}} \tag{A4}$$

Appendix B: Multi-scale triple collocation

Starting with the scale-level affine model of Eqs. (4) and (5), the associated scaling coefficients $(\alpha'_p, \alpha_{p,j})$ and error variances $(\mathrm{var}(\epsilon'_p), \mathrm{var}(\epsilon_{p,j}))$ for each scale can be estimated using TC. We use solutions of Su et al. (2014) for data triplet $p = \{X, Y, Z\}$ at each scale separately: with X as the reference by setting $\alpha_{X,j}, \alpha'_X = 1$,

$$\hat{\alpha}_{Y,j} = \frac{\mathrm{cov}(Y_j, Z_j)}{\mathrm{cov}(X_j, Z_j)}, \tag{B1}$$

$$\hat{\alpha}_{Z,j} = \frac{\mathrm{cov}(Y_j, Z_j)}{\mathrm{cov}(X_j, Y_j)}, \tag{B2}$$

$$\hat{\mathrm{var}}(\epsilon_{p,j}) = \mathrm{var}(p_j) - \frac{\mathrm{cov}(p_j, q_j)\mathrm{cov}(p_j, r_j)}{\mathrm{cov}(q_j, r_j)}, \tag{B3}$$

$$\hat{\mathrm{var}}(f_j) = \mathrm{var}(X_j) - \mathrm{var}(\epsilon_{p,j}) \tag{B4}$$

HESSD
11, 8995–9026, 2014

where q and r are also data labels, but $p \neq q \neq r$. The hat-notation is used to distinguish estimates from true values. It can be shown that, in probability, TC yields unbiased estimates whereby $\hat{\alpha}_{p,j} = \alpha_{p,j}$, $\hat{\mathrm{var}}(\epsilon_{p,j}) = \mathrm{var}(\epsilon_{p,j})$, and $\hat{\mathrm{var}}(f_j) = \mathrm{var}(f_j)$. These expressions were used to compute the results in Fig. 5 and the threshold values for wavelet de-noising. When TC does not produce physically meaningful estimates due to weak instruments, the OLS estimator was used,

$$\hat{\alpha}_{Y,j}^{\mathrm{OLS}} = \frac{\mathrm{cov}(X_j, Y_j)}{\mathrm{var}(X_j)} \tag{B5}$$

although its estimates are biased ($\hat{\alpha}_{Y,j}^{\mathrm{OLS}} < \alpha_{Y,j}$) due to the extraneous contribution of noise variance in the denominator.

Acknowledgements. We thank Wade Crow for valuable discussions and Clara Draper for her critiques on the early drafts. We are grateful to all who contributed to the data sets used in this study. Kyeamba in situ data were produced by colleagues at Monash University and the University of Melbourne who have been involved in the OzNet programme. AMSR-E data were produced by Richard de Jeu and colleagues at Vrije University Amsterdam and NASA. The MERRA-Land data set was provided by NASA Goddard Earth Sciences Data and Information Services Center (GES DISC). The land cover/use map was produced by merging land cover (Lymburner et al., 2010) and land use (Australian Bureau of Rural Science, 2010) data sets. The recalibrated precipitation data of Australian Water Availability Project (AWAP) (Jones et al., 2009) was obtained from the Australian Bureau of Meteorology. National soil data (McKenzie et al., 2005) were provided by the Australian Collaborative Land Evaluation Program ACLEP, endorsed through the National Committee on Soil and Terrain NCST (http://www.clw.csiro.au/aclep). The 9 s digital elevation map is obtained from Geoscience Australia (2008). This research was conducted with financial support from the Australian Research Council (ARC Linkage Project No. LP110200520) and the Bureau of Meteorology, Australia.

HESSD
11, 8995–9026, 2014

References

Albergel, C., De Rosnay, P., Gruhier, C., Muñoz-Sabater, J., Hasenauer, S., Isaksen, L., Kerr, Y., and Wagner, W.: Evaluation of remotely sensed and modelled soil moisture products using global ground-based in situ observations, Remote Sens. Environ., 118, 215–226, 2012. 9007

Australian Bureau of Rural Science: Land Use of Australia, version 4, 2005/2006, available at: http://data.daff.gov.au/anrdl/metadata_files/pa_luav4g9abl07811a00.xml (last access: 24 July 2014), 2010. 9015

Brocca, L., Moramarco, T., Melone, F., Wagner, W., Hasenauer, S., and Hahn, S.: Assimilation of surface- and root-zone ASCAT soil moisture products into rainfall–runoff modeling, IEEE T. Geosci. Remote, 50, 2542–2555, 2012. 8997

Caires, S. and Sterl, A.: Validation of ocean wind and wave data using triple collocation, J. Geophys. Res., 103, 3098, doi:10.1029/2002JC001491, 2003. 8997

Chang, S. G., Yu, B., and Yeterli, M.: Adaptive wavelet thresholding for imaging denoising and compression, IEEE T. Image Process., 9, 1532–1546, 2000. 9011

Daubechies, I.: Ten Lectures on Wavelets, Society for Industrial and Applied Mathematics, 1992. 9002

Donoho, D. L.: Denoising via soft thresholding, IEEE T. Inform. Theory, 41, 613–627, 1995. 9011

Donoho, D. L. and Johnstone, I. M.: Ideal spatial adaption via wavelet shrinkage, Biometrika, 81, 425–455, 1994. 8998, 9011

Draper, C., Reichle, R., De Lannoy, G., and Liu, Q.: Assimilation of passive and active microwave soil moisture retrievals, Geophys. Res. Lett., 39, L04401, doi:10.1029/2011GL050655, 2012. 8997

Drusch, M., Wood, E. F., and Gao. H.: Observation operators for the direct assimilation of TRMM microwave imager retrieved soil moisture, Geophys. Res. Lett., 32, L15403, doi:10.1029/2005GL023623, 2005. 8997

Entin, J. K., Robock, A., Vinnikov, K. Y., Hollinger, S. E., Liu, S., and Namkhai, A.: Temporal and spatial scales of observed soil moisture variations in the extratropics, J. Geophys. Res., 105, 11865–11877, 2000. 8998

Geoscience Australia: GEODATA 9-Second DEM Version 3, available at: http://www.ga.gov.au/metadata-gateway/metadata/record/66006/ (last access: 24 July 2014), 2008. 9015

HESSD
11, 8995–9026, 2014

Gruber, A., Dorigo, W. A., Zwieback, S., Xaver, A., and Wagner, W.: Characterizing Coarse-Scale Representativeness of in situ Soil Moisture Measurements from the International Soil Moisture Network, Vadose Zone J., 12, doi:10.2136/vzj2012.0170, 2013. 8997

Janssen, P. A. E. M., Abdalla, S., Hersbach, H., and Bidlot, J.-R.: Error estimation of buoy, satellite, and model wave height data, J. Atmos. Ocean. Tech., 24, 1665–1677, 2007. 8997

Jones, D. A., Wang, W., and Fawcett, R.: High-quality spatial climate data-sets for Australia, Aust. Meteorol. Oceanogr., 58, 233–248, 2009. 9015

Koster, R. D., Guo, Z., Yang, R., Dirmeyer, P. A., Mitchell, K., and Puma, M. J.: On the nature of soil moisture in land surface models, J. Climate, 22, 4322–4335, 2009. 9007

Kumar, S. V., Reichle, R. H., Harrison, K. W., Peters-Lidard, C. D., Yatheendradas, S., and Santanello, J. A.: A comparison of methods for a priori bias correction in soil moisture data assimilation, Water Resour. Res., 48, W03515, doi:10.1029/2010WR010261, 2012. 8997

Legates, D. R., Mahmood, R., Levia, D. F., DeLiberty, T. L., Quiring, S. M., Houser, C., and Nelson, F. E.: Soil moisture: a central and unifying theme in physical geography, Prog. Phys. Geogr., 35, 65–86, 2011. 8997

Liu, Y. Y., Dorigo, W. A., Parinussa, R. M., De Jeu, R. A. M., Wagner, W., McCabe, M. F., Evans, J. P., and Van Dijk, A. I. J. M.: Trend-preserving blending of passive and active microwave soil moisture retrievals, Remote Sens. Environ., 123, 280–297, 2012. 8998

Lymburner, L., Tan, P., Mueller, N., Thackway, R., Lewis, A., Thankappan, M., Randall, L., Islam, A., and Senarath, U.: 250 metre Dynamic Land Cover Dataset of Australia, 1st edn., Geoscience Australia, Canberra, 2010. 9015

Mallat, S. G.: A theory for multiresolution signal decomposition: the wavelet representation, IEEE T. Pattern Anal., 11, 674–693, 1989. 8998, 9002

McKenzie, N. J., Jacquier, D. W., Maschmedt, D. J., Griffin, E. A., and Brough, D. M.: The Australian Soil Resource Information System: Technical Specifications, National Committee on Soil and Terrain Information/Australian Collaborative Land Evaluation Program, Canberra, 2005. 9015

Miralles, D. G., De Jeu, R. A. M., Gash, J. H., Holmes, T. R. H., and Dolman, A. J.: Magnitude and variability of land evaporation and its components at the global scale, Hydrol. Earth Syst. Sci., 15, 967–981, doi:10.5194/hess-15-967-2011, 2011. 8997, 8998, 9007

Mittelbach, H. and Seneviratne, S. I.: A new perspective on the spatio-temporal variability of soil moisture: temporal dynamics versus time-invariant contributions, Hydrol. Earth Syst. Sci., 16, 2169–2179, doi:10.5194/hess-16-2169-2012, 2012. 8998

HESSD
11, 8995–9026, 2014

Owe, M., de Jeu, R., and Holmes, T.: Multisensor historical climatology of satellite-derived global land surface moisture, J. Geophys. Res., 113, F01002, doi:10.1029/2007JF000769, 2008. 8999

Peel, M. C., Finlayson, B. L., and McMahon, T. A.: Updated world map of the Köppen–Geiger climate classification, Hydrol. Earth Syst. Sci., 11, 1633–1644, doi:10.5194/hess-11-1633-2007, 2007. 9000

Reichle, R. H. and Koster, R. D.: Bias reduction in short records of satellite soil moisture, Geophys. Res. Lett., 31, L19501, doi:10.1029/2004GL020938, 2004. 8997, 9006

Reichle, R. H., Koster, R. D., Dong, J., and Berg, A. A.: On global soil moisture from satellite observations, land surface models, and ground data: implications for data assimilation, J. Hydrometeorol., 5, 430–442, 2004. 8997

Reichle, R. H., Koster, R. D., Liu, P., Mahanama, S. P. P., Njoku, E. G., and Owe, M.: Comparison and assimilation of global soil moisture retrievals from the Advanced Microwave Scanning Radiometer for the Earth Observing System (AMSR-E) and the Scanning Multichannel Microwave Radiometer (SMMR), J. Geophys. Res., 112, D09108, doi:10.1029/2006JD00803, 2007. 8997

Reichle, R. H., Koster, R. D., De Lannoy, G. J. M., Forman, B. A., Liu, Q., Mahanama, S. P. P., and Touré, A.: Assessment and enhancement of MERRA land surface hydrology estimates, J. Climate, 24, 6322–6338, 2011. 9000

Rienecker, M. M., Suarez, M. J., Gelaro, R., Todling, R., Bacmeister, J., Liu, E., Bosilovich, M. G., Schubert, S. D., Takacs, L., Kim, G.-K., Bloom, S., Chen, J., Collins, D., Conaty, A., da Silva, A., Gu, W., Joiner, J., Koster, R. D., Lucchesi, R., Molod, A., Owens, T., Pawson, S., Pegion, P., Redder, C. R., Reichle, R., Robertson, F. R., Ruddick, A. G., Sienkiewicz, M., and Woollen, J.: MERRA – NASA's Modern-Era Retrospective Analysis for Research and Applications, J. Climate, 24, 3624–3648, 2011. 9000

Rodrigeuz-Iturbe, I.: Ecohydrology: a hydrologic perspective of climate-soil-vegetation dynamics, Water Resour. Res., 36, 3–9, 2000. 8996

Roebeling, R. A., Wolters, E. L. A, Meirink, J. F., and Leijnse, H.: Triple collocation of summer precipitation retrievals from SEVIRI over Europe with gridded rain gauge and weather radar data, J. Hydrometeorol., 13, 1552–1566, 2013. 8997

Scipal, K., Drusch, M., and Wagner, W.: Assimilation of a ERS scatterometer derived soil moisture index in the ECMWF numerical weather prediction system, Adv. Water Resour., 31, 1101–1112, 2008a. 8997

HESSD

11, 8995–9026, 2014

Scipal, K., Holmes, T., de Jeu, R., Naeimi, V., and Wagner, W.: A possible solution for the problem of estimating the error structure of global soil moisture data sets, Geophys. Res. Lett., 35, L24403, doi:10.1029/2008GL035599, 2008b. 8997

Smith, A. B., Walker, J. P., Western, A. W., Young, R. I., Ellett, K. M., Pipunic, R. C., Grayson, R. B., Siriwardena, L., Chiew, F. H. S., and Richter, H.: The Murrumbidgee soil moisture network data set, Water Resour. Res., 48, W07701, doi:10.1029/2012WR011976, 2012. 8999

Stoffelen, A.: Towards the true near-surface wind speed: Error modelling and calibration using triple collocation, J. Geophys. Res., 103, 7755–7766, 1998. 8997

Su, C.-H., Ryu, D., Young, R. I., Western, A. W., and Wagner, W.: Inter-comparison of microwave satellite soil moisture retrivals over Murrumbidgee Basin, southeast Australia, Remote Sens. Environ., 134, 1–11, 2013. 8997, 8999

Su, C.-H., Ryu, D., Crow, W. T., and Western, A. W.: Beyond triple collocation: applications to satellite soil moisture, J. Geophys. Res.-Atmos., 119, 6419–6439, 2014. 8997, 8998, 9004, 9005, 9006, 9007, 9014

The GLACE Team, Koster, R. D., Dirmeyer, P. A., Guo, Z., Bonan, G., and Chan, E.: Regions of strong coupling between soil moisture and precipitation, Science, 305, 1138–1140, 2004. 8996

Wang, G., Garcia, D., Liu, Y., de Jeu, R., and Dolman, A. J.: A three-dimensional gap filling method for large geophysical datasets: application to global satellite soil moisture observations, Environ. Modell. Softw., 30, 139–142, 2012. 9000

Western, A. W., Grayson, R. B., and Bloschl, G.: Scaling of soil moisture: a hydrologic perspective, Annu. Rev. Earth Pl. Sc., 30, 149–180, 2002. 8997

Wright, P. G.: The Tariff on Animal and Vegetable Oils, Macmillan, New York, 1928. 8997

Yilmaz, M. T. and Crow, W. T.: The optimality of potential rescaling approaches in land data assimilation, J. Hydrometeorol., 14, 650–660, 2013. 8997, 9006

Zwieback, S., Scipal, K., Dorigo, W., and Wagner, W.: Structural and statistical properties of the collocation technique for error characterisation, Nonlinear Proc. Geoph., 19, 69–80, 2012. 9005

HESSD

11, 8995–9026, 2014

Table 1. RMSD (in units of $m^3\ m^{-3}$) and correlation between INS and AMS at Kyeamba treated by various methods. The square brackets contain 95 % confidence interval.

Methods	RMSD	Correlation
None	0.088	0.659[14]
Bulk linear	0.055	0.659[14]
Bulk CDF	0.053	0.679[14]
A/S linear	0.059	0.635[15]
A/S CDF	0.054	0.671[14]
Multi-scale (MS)	0.062	0.650[15]
Wavelet thres. (WT)	0.069	0.709[13]
WT + MS	0.048	0.711[12]

HESSD
11, 8995–9026, 2014

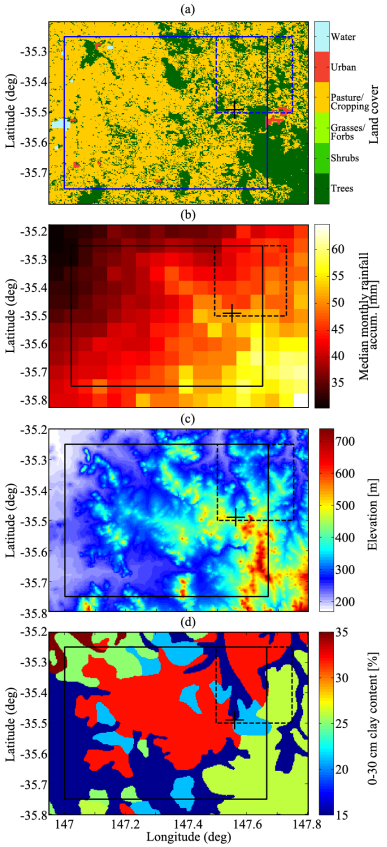

Figure 1. Spatial variability of land surface and rainfall over Kyeamba Creek. The cross denotes the location of the K1 monitoring station, and the dashed (solid) box is the pixel area of AMS (MER).

HESSD
11, 8995–9026, 2014

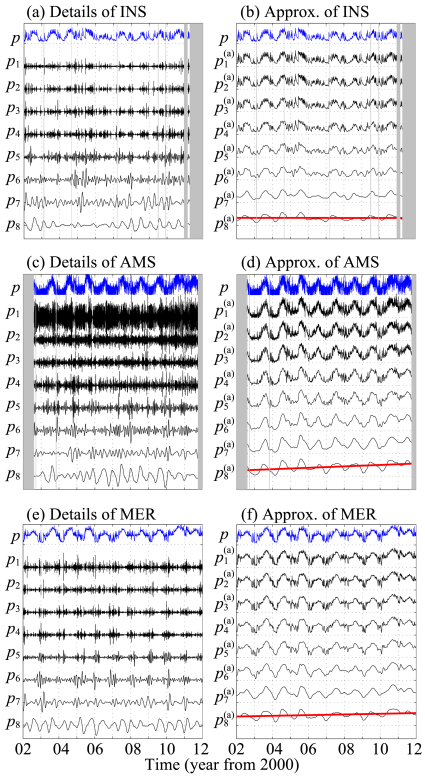

Figure 2. MRA of INS, AMS and MER SM at Kyeamba. Grey shadings are > 5 day data gaps, and red lines are trend lines fitted to $p_8^{(a)}$.

HESSD
11, 8995–9026, 2014

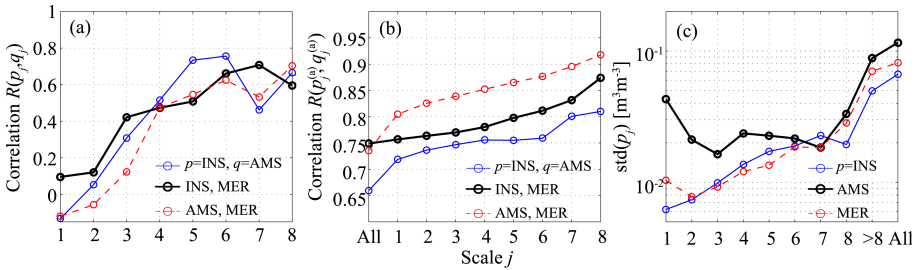

Figure 3. Comparisons of correlation and std between INS, AMS and MER at scale levels. Scale $j > 8$ corresponds to $p_8^{(a)}$, and "All" refers to statistics of the original timeseries.

HESSD
11, 8995–9026, 2014

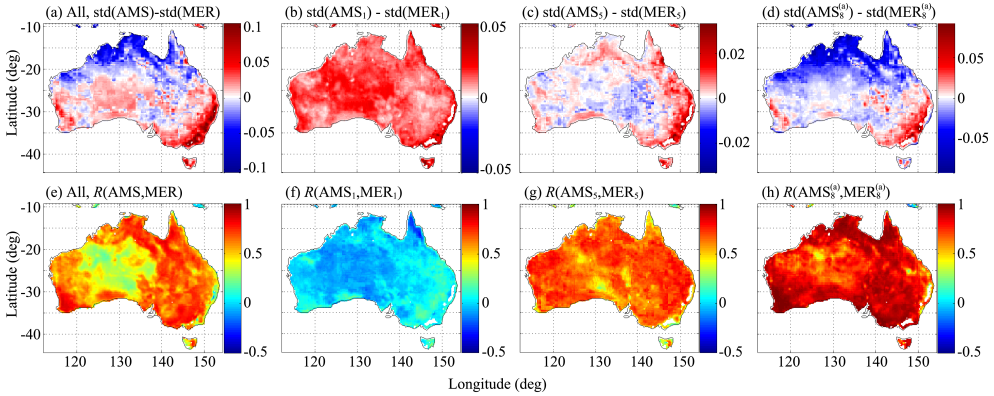

Figure 4. Difference in std (in units of $m^3\ m^{-3}$) and correlation R between AMS and MER for **(a, e)** all, and (rest) at selected time scales.

HESSD
11, 8995–9026, 2014

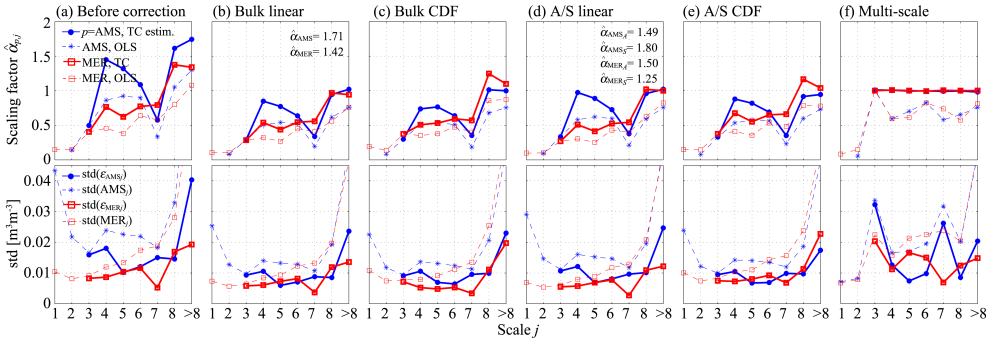

Figure 5. Responses of the scaling coefficients $\alpha_{Y,j}$ (of AMS and MER with respect to INS), noise and total std at individual scales to 5 bias correction schemes. **(a)** is the analysis for untreated AMS and MER (as Y) and **(b–f)** are that for Y^* after correction. Two estimators, TC and OLS, were applied to estimate $\alpha_{Y,j}$. The $\hat{\alpha}$ values listed in **(b, d)** are the scaling coefficients used in the associated implementations. Scale $j > 8$ corresponds to $Y_8^{(a)}$

HESSD
11, 8995–9026, 2014

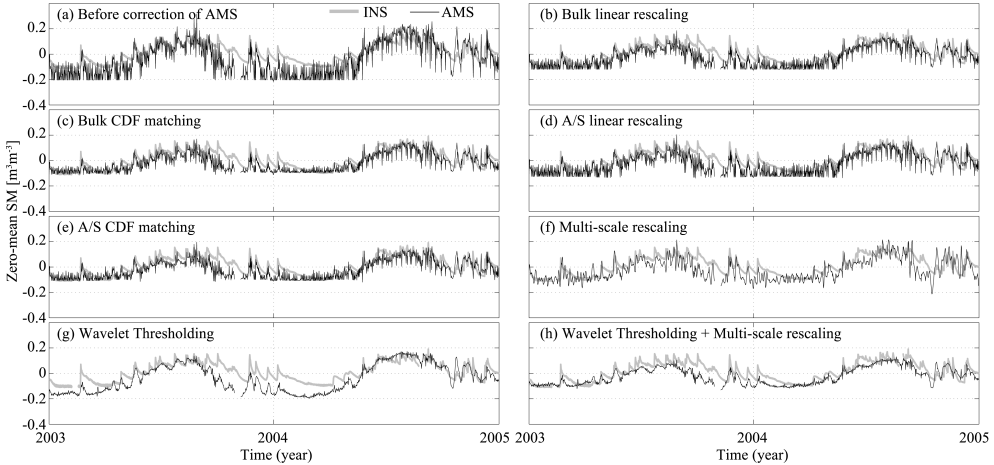

Figure 6. Timeseries of AMS SM treated by various bias correction schemes.

HESSD
11, 8995–9026, 2014